



Max-Planck-Institut für  
extraterrestrische Physik



# PERFORMANCE OF A SPACE-BASED TELESCOPE FOR COSMIC GAMMA-RAYS

---

PERFORMANZ EINES WELTRAUMBASIERTEN  
GAMMASTRAHLEN-TELESKOPS

## B A C H E L O R A R B E I T

zur Erlangung des Grades eines 'Bachelor of Science'  
im Fachbereich Kern-, Teilchen- und Astrophysik  
der Technischen Universität München

eingereicht am

18. September 2017

bei

Prof. Dr. rer. nat. Roland Diehl

Max-Planck-Institut für Extraterrestrische Physik

von

Benjamin Johann Hafensteiner

Matrikelnummer: 03659165

Schornstraße 15

81669 München

# Declaration

I warrant that I made this work independently and that I have not received outside assistance. Parts that are direct quotes or paraphrases are identified as such.

Ich versichere, dass ich die vorliegende Arbeit selbstständig angefertigt und mich keiner fremden Hilfe bedient habe. Alle Stellen, die wörtlich oder sinngemäß veröffentlichtem oder unveröffentlichtem Schrifttum entnommen sind, habe ich als solche kenntlich gemacht.

München, 18.09.2017

---

Benjamin Johann Hafensteiner

## Contents

<b>1</b>	<b>Introduction</b>	<b>1</b>
<b>2</b>	<b>The INTEGRAL Mission</b>	<b>3</b>
2.1	Composition of the Satellite . . . . .	3
2.2	Achievements . . . . .	4
<b>3</b>	<b>Event Detection with SPI</b>	<b>5</b>
3.1	Composition of the Spectrometer . . . . .	5
3.2	Germanium Detectors . . . . .	6
3.2.1	Functionality . . . . .	6
3.2.2	Performance . . . . .	6
3.2.3	Cooling System Cryostat . . . . .	9
3.2.4	Annealing . . . . .	10
3.3	Background Reduction . . . . .	10
3.3.1	Anticoincidence Shield . . . . .	10
3.3.2	Pulse Shape Discrimination Electronics . . . . .	11
3.3.3	Plastic Scintillator Anticoincidence Subassembly . . . . .	11
<b>4</b>	<b>Energy Calibration</b>	<b>13</b>
4.1	General Considerations . . . . .	13
4.1.1	Fitting Data . . . . .	13
4.1.2	Error Propagation . . . . .	14
4.1.3	Defining Peak Positions . . . . .	15
4.1.4	Weighting Mean Values . . . . .	17
4.1.5	Linear Regression . . . . .	17
4.2	Calibration Procedure . . . . .	18

---

<b>5</b>	<b>Analysis of Data</b>	<b>22</b>
5.1	Comparing Calibrations over Time . . . . .	22
5.2	Calibration Adjustments . . . . .	23
5.3	Characteristics of the Peak Positions . . . . .	25
5.4	Line Identification . . . . .	26
5.5	Correlation of Energy and Increasing Values of Peak Positions . . . .	28
<b>6</b>	<b>Conclusion</b>	<b>30</b>
<b>7</b>	<b>Danksagung</b>	<b>31</b>

## 1 Introduction

The satellite INTEGRAL (short for **INTE**rnational **G**amma-**R**ay **A**strophysics **L**aboratory) was launched on October 17, 2002, in Kazakhstan. Already in 1993, the European Space Agency has selected INTEGRAL as their next medium size mission.

It's goal is the investigation of the entire celestial sphere in order to gain a better understanding of it. This is done by measuring gamma-rays, which are defined as photons with an energy above  $\sim 200$  keV. Other than cosmic rays, that contain mainly protons, but also electrons or fully ionized atoms, gamma-rays do not get diverted by the magnetic field of stars. Thus they provide meticulous information about their source location. Further knowledge about our cosmos can be gained by analysing them, for example how big a certain star is or which metals the star contains.

Because earth's atmosphere blocks gamma-rays, efficient detection can only take place outside the atmosphere with satellites that orbit above it. Besides the atmosphere, the earth is enclosed by a radiation belt, called Van Allen belt, a zone of energetic charged particles, that are captured by the magnetic field of the earth. There are two of these Van Allen belts surrounding the earth. The inner radiation belt extends from an altitude of 1000 km to 6000 km, the outer radiation belt from 13000 km to 60000 km. In order to avoid a prolonged stay in the radiation belts, that would influence the measurements, Integrals orbit was chosen highly eccentric, with an apogee of  $\sim 157000$  km and an perigee of  $\sim 6000$  km. Its revolving period is 72 h 5 min, hence only slightly more than 3 days.

The main source of gamma-rays is penetrating electromagnetic radiation that occurs when atomic nuclei decay radioactively. Further sources of gamma-rays are Compton scattering, bremsstrahlung or electron-positron annihilation.

Originally, INTEGRAL was selected to be decommissioned after 5 years, due to it's excellent performance though the mission was extended for another 5 years, and ever since for 2 years each, currently running until December 31, 2018.

Among other (highly developed) instruments, on board INTEGRAL there is a sensitive gamma ray telescope, called SPI (Spectrometer on INTEGRAL), that measures in the range of 18-8000 keV. To accomplish this, a detector array of 19 germanium detectors with ultra high sensitivity is utilized.

This enables INTEGRAL, or more precisely SPI, to draw spectra from gamma-ray emitting sources that are scattered all over the universe. These spectra consist of characteristic lines, that originate from the photoelectric effect, the Compton effect and pair production, and also an underlying continuum. These high energy sources are supernovae, black holes, neutron stars and gamma-ray bursts. Because this radiation constantly impinges the detectors (and the other instruments), their efficiency decreases over time. For that reason twice a year the detectors are heated

up with the goal of restoring their original efficiency.

A major challenge of gaining usable data with SPI is the great presence of background noise, that originates from different materials of the installed instruments that also lead to the emission of gamma-rays. Although there are veto shields installed on board INTEGRAL, only about 1 % of the detected photons have their origin in the celestial sphere. Therefore, it is of crucial importance to be able to differentiate between photons coming from celestial sources and the ones coming from the instruments themselves. Another challenge is to turn raw spectra into useful data. To achieve this, a carefully conducted energy calibration is essential. The initial data are just events that trigger the germanium detector and create an electronic pulse. Thereupon the pulse heights are digitized and saved in channels for ensuing spectral analysis. The amplitude of each pulse contains information of the charge that originated from that particular interaction that took place in the detector. In the obtained spectra,  $\sim 380$  lines that stick out from the continuum can be seen. Some lines were found to be very strong (for their respective energy), and six of those strong lines were chosen as calibration lines, that are used to calculate a correlation between channel number and energy, since the energies of the transitions are known.

One topic is to explain how this energy calibration is done and what challenges have to be faced, and also to classify how precise the calibration is and if there are possibilities to improve it.

Moreover, in order to provide a better understanding of the physical basis, a calibration will be performed and compared to an already existing one. After the calibration has been applied, one can now extract information about energy peaks. In this thesis the centroid of some of the lines with high count rates compared to other lines will be under investigation. Particularly, it will be looked at their behaviour in between the annealing phases and conclusions of that will be drawn.

## 2 The INTEGRAL Mission

### 2.1 Composition of the Satellite

The payload of INTEGRAL consists of four instruments called IBIS (**I**mager on **B**oard the **I**ntegral **S**atellite), SPI (**S**Pectrometer on **I**ntegral), JEM-X (**J**oint **E**uropean **X**-Ray **M**onitor) and OMC (**O**ptical **M**onitoring **C**amera). The satellite is 5 m long and has a diameter of 3.2 m.

The apertures of both the SPI spectrometer and the IBIS imager employ coded masks for imaging, and both instruments analyse gamma-ray source location between 18 keV and 8 MeV. The two monitor instruments complement the INTEGRAL instrumentation, the JEM-X addressing lower energies with a wider field of view and the OMC for simultaneous optical exposure of the target sky regions (Diehl 2013).

All four instruments survey the same area of the universe contemporaneously to make complementary diagnosis of high-energy sources.

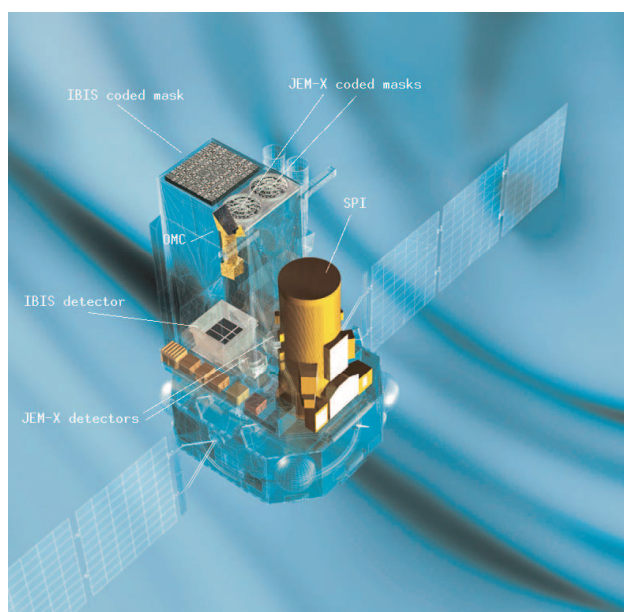


Figure 1: INTEGRAL spacecraft. Dimension are (5x2.8x3.2)m. The deployed solar panels are 16 meter across. The mass is 4t (at launch), including 2t of payload. (Winkler et al. 2003)

The data under investigation subsequently will be exclusively data obtained by the SPI spectrometer.

One of the main tasks in high energy astrophysics is the reduction of the background noise. This noise appears because gamma rays interact with the material of the

instrument and other spacecraft materials, which leads to the emission of photons. These photons are additionally detected to the photons originating from the sky. This means that for surveys of the sky this instrumental background has to be subtracted. Since the background noise is very dominant, a series of sub-assemblies have been installed on INTEGRAL, that reduce this background noise a considerably (Weidenspointner et al. 2003).

A more in depth description of SPI's functionality and it's sub-assemblies will be given in the section 'Event detection with SPI'.

## 2.2 Achievements

INTEGRAL enables scientists to study our universe at gamma-ray wavelengths, and its mission would not have been extended several times, if there had not been a large list of observations during its period of validity. Because this is not the focus of this thesis, just a few are listed below.

In 2005 one of the fastest spinning neutron stars, named XTE J1739-285, has been discovered. The star is spinning 1122 times per second. Neutron star material has a density of  $\sim 10^{15} \frac{g}{cm^3}$ .

INTEGRAL has also made the first unambiguous discovery of highly energetic X-rays coming from the galaxy cluster known as Ophiuchus. The emission is thought to originate from giant shock-waves rippling through the cluster's gas as two galaxies collide and merge. (Eckert et al. 2008)

INTEGRAL has also been probing the feeding habits of active galaxies and black holes, which lurk in the centre of most galaxies, including our own. Many super-massive black holes are surrounded by thick dust discs, which INTEGRAL can peer through to identify the black hole hidden within.

SPI's measurements of the radial velocities of radioactive  $^{26}\text{Al}$  allow to trace the kinematics of cumulative massive-star and supernova ejecta. Since  $^{26}\text{Al}$  has a mean lifetime of 1.04 Myr, this can be done for million-year time scales, independent of the undetermined gas parameters (Kretschmer et al. 2013). Furthermore, the study of  $^{26}\text{Al}$  emission in spatially-restricted regions along the plane of the galaxy lead to interesting results, for example that the disk of our galaxy is not azimuthally-symmetric (Wang et al. 2009).

In 2014 INTEGRAL observed gamma-ray lines of a supernova that could confirm that white dwarfs are able to reignite and explode.

Above this INTEGRAL provides through the big amount of data collected since its launch unique insights in the functionality of gamma-ray spectroscopy and gamma-ray behaviour and the analysis of this legacy database is a task that can easily exceed the time period INTEGRAL remains in orbit.

### 3 Event Detection with SPI

#### 3.1 Composition of the Spectrometer

The **SP**ectrometer on **INTEGRAL** is a high spectral resolution gamma-ray telescope. It has an energy range from 18 keV up to 8 MeV and consists of 19 germanium detectors with a detector area of 500 cm<sup>2</sup>. SPI's spectral resolution lies at 3 keV at 1.7 MeV, while the angular resolution is 2.5°.

SPI's fully coded field of view, the sky region from where any source would cast a shadow of the coded mask that would cover the entire detector area, is with 16° quite large. SPI's total mass amounts to 1309 kg and it operates with a maximum power of 385 W and an average power of 110 W.

The camera of SPI consists of 19 hexagonal, n-type germanium detectors, with a weight of 18 kg.

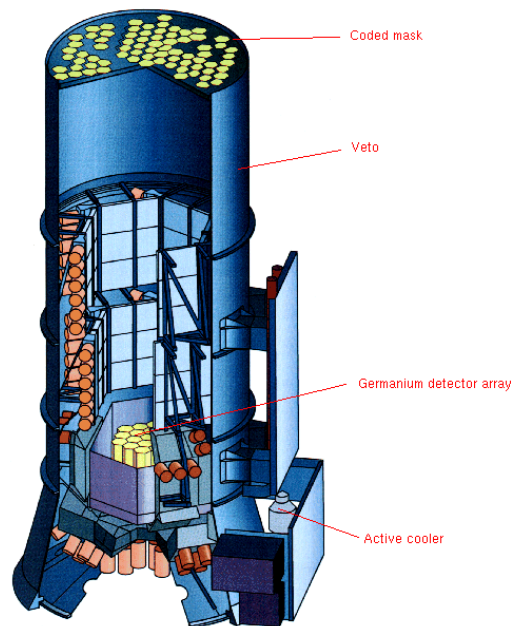


Figure 2: illustration of the Spectrometer aboard INTEGRAL

## 3.2 Germanium Detectors

### 3.2.1 Functionality

Germanium detectors are semiconductor detectors. Semiconductors are solid materials that have electrical conductivity between a conductor and an insulator. The valence band and the conduction bands are separated typically by about 1 eV. The energy of the gamma rays is proportional to and thus measured by the amount of charge carriers that are set free in the detector material. The gamma-

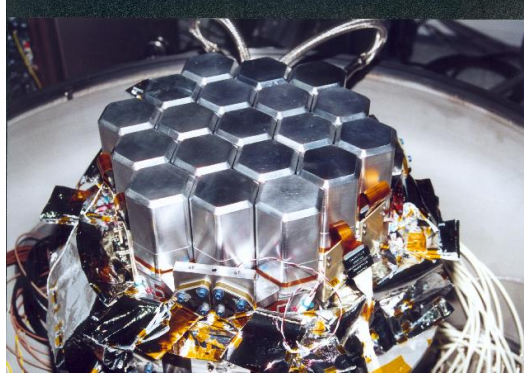


Figure 3: picture of the detector array aboard INTEGRAL

rays excite electrons from the valence band up into the conduction band, leaving an equal amount of vacant states, named holes, in the valence band behind. These holes are filled by another electron, creating a new hole on the electrons former position. Consequently, they behave like positive charged particles. Through an electric field, the electrons and holes in the conduction band travel to the electrodes, where they create a pulse that can be measured. Since the band gap is very narrow, also thermal energies can excite electrons up into this conduction band easily, but this is unfavoured since this produces too much electrical noise. For this reason, the semiconducting material is cooled down to liquid nitrogen temperatures, so that only electrons originating from interactions with gamma rays are able to reach the conduction band. The small band gap of the germanium detectors leads to a larger number of charge carriers, providing better count statistics.

### 3.2.2 Performance

Above several hundred keV, only two detector types play a prominent role. The first are inorganic scintillators, the second are germanium semiconductor detectors. Usually for semiconductor detectors nowadays silicon is preferred, but the higher melting point for silicon (1410°C versus 959°C) makes the exclusion of impurities in the refining process more difficult. The impurity level of the used germanium crystals has been set to be between  $5 \cdot 10^9 \text{ cm}^{-3}$  and  $1.5 \cdot 10^{10} \text{ cm}^{-3}$  and is therefore qualified as ultra-pure germanium.

When choosing a certain type of detector, a careful consideration of weighing up the importance between counting efficiency and energy resolution has to be made. The latter is given by the equation

$$R = \frac{FWHM}{H_0} \quad (1)$$

with the full width at half maximum FWHM and the mean value  $H$ . For Gaussian shaped peaks with the Standard deviation of  $\sigma$ , the FWHM is given by

$$FWHM = 2.35\sigma \quad (2)$$

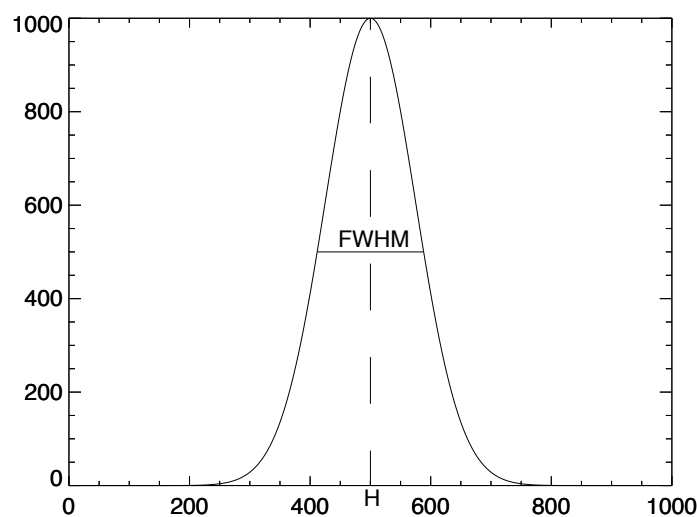


Figure 4: Full Width at Half Maximum

From equation 1 follows that the energy resolution is dimensionless, consequently it is conventionally expressed as a percentage. Because germanium detectors have a very high energy resolution compared to other detector types, they are undoubtedly favoured for the examination of complex gamma-ray spectra, that usually consist of a lot of lines that should be distinguishable. The meaning of high energy resolution is graphically illustrated in figure 5.

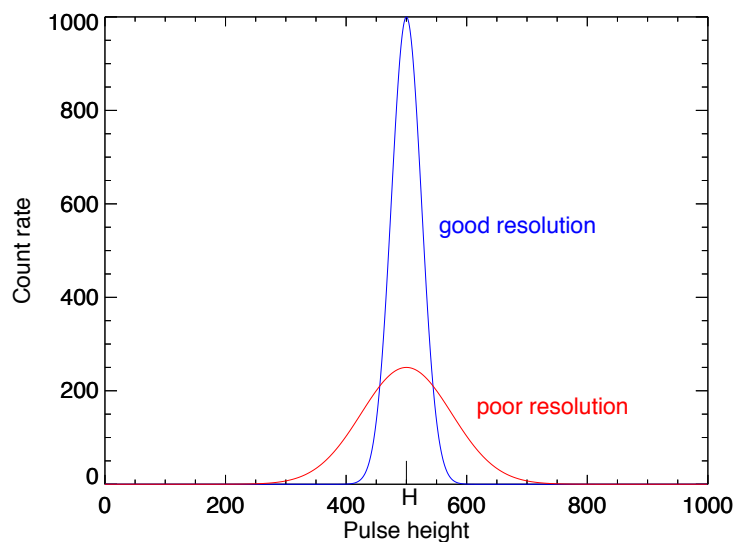


Figure 5: Comparison of good and poor resolution

Well functioning germanium detectors typically operate with an energy resolution of a few tenths of a percent (Knoll 2012).

SPI's stated energy resolution of 2.2 keV at 1.33 MeV meets this requirement.

By observing the spectra of the individual detectors, one can see that 4 of the 19 detectors broke down, leaving 15 working. This happened for detector 2 in revolution 140, for detector 17 in revolution 214, for detector 5 in revolution 774 and for detector 1 in revolution 929. Their spectra simply breaks off at this point, as shown in figure 6. The spectrum of detector 18 has also been included (black coloured spectrum), representative for a detector that is still functioning well.

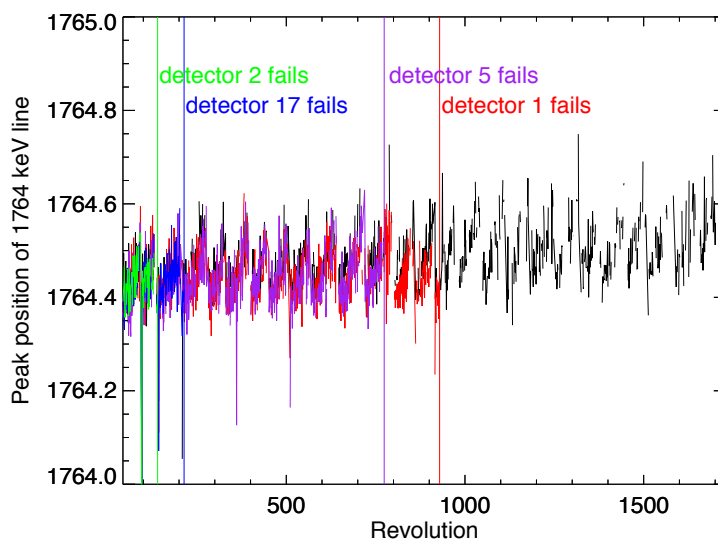


Figure 6: Detector breakdowns

### 3.2.3 Cooling System Cryostat

As mentioned in chapter 3.2.1, the germanium detectors need to be cooled down to liquid nitrogen temperatures to be useful for gamma-ray spectroscopy. This is done by the cryostat with the aid of four mechanical Stirling cycle coolers.

Because the performance of the mechanical coolers is limited to a few Watts, the detectors have to be very well thermally insulated from their environment. That is why the detector plane is embedded in a so called Cold Box consisting of beryllium, that is kept at 210 K by a passive cooling device. The Cold Box is connected to an external radiator, on which the four coolers are mounted,

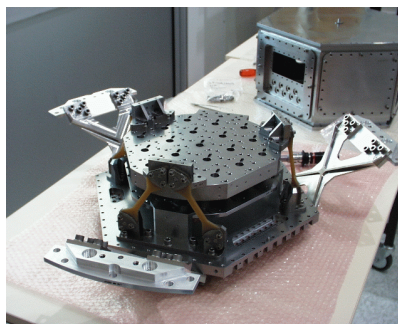


Figure 7: Picture of the cryostat aboard INTEGRAL

via two ammonia-filled heat pipes. Because their necessary power usage is proportional to their temperature, it is reasonable to keep them at low temperatures, thus around the ammonia freezing point, which is at 196K. For the case that the ammonia freezes, a heat pipe has also been installed to thaw the pipes, if required. The detectors themselves are kept at 85-90 K, connected to the coolers via a Cold Rod called cold finger. (Vedrenne et al. 2003)

All together the cryostat's weight is 80 kg, without the detectors though, which would add another 22 kg.

### 3.2.4 Annealing

Due to cosmic radiation the germanium detectors get constantly damaged. These damaging cosmic rays are mostly highly energetic protons and neutrons. By interacting with Ge atoms, they can damage the structure of the germanium. This has the consequence that over time the original lattice structure gets more and more unstructured, which results in a decrease of the detector resolution. For this reason the detectors are heated up to 105°C twice a year for one or two weeks, so that induced by thermal movement the molecules can relocate themselves afterwards and fill the holes in the existing lattice again as they are cooling down. During these annealing phases it is not possible to make any valuable measurements. So far, 27 annealing processes have been successfully carried out, restoring a great amount of the detectors original performances.

## 3.3 Background Reduction

One of the main challenges when collecting data is the high existence of background radiation. In fact, the data measured by the detectors consists of about 99 percent of background radiation, which is however of no value for our analyses. There are a few instruments installed on SPI with the purpose of reducing the massive amount of background radiation.

### 3.3.1 Anticoincidence Shield

The by far most important sub-assembly to reduce background is the large hexagonal **Anti Coincidence Shield (ACS)**. The shield is surrounding the germanium detector and thus shielding them against background radiation from nearly all sides. It contains 91 bismuth germanium oxid (BGO) scintillator crystals, that have a volume of  $\sim 790 \text{ cm}^2$  piece by piece, combined with photo multiplier tubes. Overall the mass of BGO that is implemented in the ACS amounts to 512 kg. All events coming in are converted by the scintillator crystals into photons in the 480 nm region, which corresponds to the range of visible light. In consideration of detecting these photons,

photo-multiplier tubes, that multiply the current produced by incident light up to 100 million times, are utilized and the photons are converted into electrical pulses, which are sorted, normalized and summed up by the ACS electronics. When a photon is registered by the ACS, a veto signal is sent to the Digital Front End Electronics (DFEE) and it will veto any detector events that occur at the same time. (*Anti Coincidence Shield*)

Since the energy-threshold is not very sharp, it is broadened over an energy range of the order of 100 keV, and it has to be weighed up whether background reduction or reduction of the dead time for the SPI camera should be favoured. Concurrently with the commissioning phase, a threshold setting of about 75 keV has been set, which seems to be an optimal adjustment. Shielding is not the only function of the ACS. It is also valuable in the sense that it provides a vast effective area for the detection of gamma-bursts (Vedrenne et al. 2003). Unfortunately it provides only poor positional information of about  $\sim 60^\circ$  though.

### 3.3.2 Pulse Shape Discrimination Electronics

The **Pulse Shape Discrimination (PSD)** electronics task is to reduce the instrumental background in the energy range of 200 - 2000 keV. In this realm the dominant background components have their origin in localised beta decays, that occur without the emission of a gamma-ray photon. The energy deposit of the beta decays is limited to a few mm, in contrast to the gamma-rays, that typically have their origin in Compton scattering, leading to multiple interaction inside the detector area. For all events PSD is checking the present pulse shape of the signal in the electrodes and then commanding it to an investigation in order to analyse if the interaction that took place in the detector occurred on only one, and no other, input channel. The input current gets digitized for  $\sim 1 \mu\text{s}$  with a time resolution of  $\sim 10 \text{ ns}$ , which is enough to get data points of the pulse that have normally a duration of  $\sim 300 \text{ ns}$  and also enough to determine the baseline current. (Vedrenne et al. 2003)

When investigating a larger amount of pulses, their individual amplitudes will differ. This can occur because of differences in the energy of the radiation or fluctuations in the detectors inherent response to mono-energetic radiation (Knoll 2012).

### 3.3.3 Plastic Scintillator Anticoincidence Subassembly

The **Plastic Scintillator Anticoincidence Subassembly (PSAC)** is located beneath the mask. More precisely it is installed inside a light diffusion chamber that yields a homogeneous distribution of photons originating from particle interaction in the thin plastic scintillator. The PSAC is 5 mm thick and has a diameter of 800 mm, the light diffusion chamber is of 106 mm height and 826 mm in diameter.

PSACs goal is the minimization of the background specifically for the 511 keV energy range. (Vedrenne et al. 2003)

## 4 Energy Calibration

Because the 'raw spectra' consist only of the number of photons detected plotted against the channel numbers, we have to modify it by applying an energy calibration. In the raw spectra there are several characteristic lines, which are used for the calibration. To be more precise, the energy levels will be assigned to their corresponding channel numbers through the calibration function

$$E(x) = \frac{a_0}{x} + a_1 + a_2 * x + a_3 * x^2 \quad (3)$$

that has been used by the INTEGRAL Science Data Centre (ISDC). In the calibration function the unit of  $E(x)$  is keV and  $x$  are the channel numbers (or pulse heights), that range from 1-16384. The energy values are taken from the physical processes of the isotopes (Weidenspointner et al. 2003) that are most likely to be the origin of the reference line centroids measured in the channel space.

After some general considerations, the calibration of detector 0 and revolution 45 will be examined.

### 4.1 General Considerations

#### 4.1.1 Fitting Data

For practical reasons it is often of great interest to fit a 'model' that depends on adjustable parameters to the data. In order to classify how valid our model is, a chosen figure-of-merit function, that shows the deviation between the data and the model should be used. Of course, this deviation is desired to be as small as possible, and the merit function is conventionally designed in the way that small values of the merit function indicate close consensus between the data and the model.

Because typically data will never match the used model completely, there has to be a way to classify the goodness-of-fit. This is shown by the value  $\chi^2$  or rather the  $\chi^2_\nu$  (reduced Chi square).  $\chi^2$  is commonly used for fitting model to data, and given a general function  $y(x_i; a_0, a_1 \dots a_M)$  with  $M$  adjustable parameters, the  $\chi^2$  value originates mathematically from the equation:

$$\chi^2 \equiv \sum_{i=1}^N \left( \frac{y_i - (y(x_i; a_0, a_1 \dots a_M))}{\sigma_i} \right)^2 \quad (4)$$

$y_i$  are the data points, and  $y(x_i; a_0, a_1 \dots a_M)$  is the fit function.  $\sigma_i$  in general is the measurement error, and in case of Poisson distributed measurements it is the standard deviation of the data point  $(x_i, y_i)$ . For low values of  $\chi^2$ , the numerator

has to be small as well. This is the case when the parameters  $y(x_i; a_0, a_1 \dots a_M)$  are adjusted in the way that the deviation between the measured data and the fit function is small, which indicates a close agreement between them and therefore the fit can consequently be classified as good.

$$\chi_\nu^2 = \frac{\chi^2}{\nu} \quad (5)$$

$\chi_\nu^2$  is defined as  $\chi^2$  per degree of freedom  $\nu$ . The latter is given by  $\nu = N - V$  with  $V$  being the number of the fitting parameters (Press et al. 1995). A rule of thumb is that for values of  $\chi_\nu^2 \gg 1$  the fit is not good enough to describe the data accurately, values  $> 1$  imply that the fit is rather poor, and values of  $\sim 1$  signify that the extent of the match between measurement and fit is in line with the error variance.

In the case of SPI, equation 4 forms to

$$\chi^2 \equiv \sum_{i=1}^N \left( \frac{y_i - (y(x_i; a_0, a_1, a_2, a_3))}{\sigma_i} \right)^2 \quad (6)$$

Here  $y_i$  are the actually measured data points by SPI, and  $y(x_i; a_0, a_1, a_2, a_3)$  is the calibration function given by equation 3.

The previously conducted calibrations were done by the ISDC. In order to fit the peak positions, a symmetric Gaussian fit was chosen by ISDC. Subsequently, it will be proven though that asymmetric Gaussian fits are more accurate, which is shown in a lower value of  $\chi^2$ . To determine how much more significant the asymmetric fits are, the  $\chi^2$ -test will be used, a comparison of the  $\chi^2$ -values taking into account the degrees of freedom.

For the asymmetric Gaussian fits the Monte Carlo Markov Chain (MCMC) was used. We have 6 starting parameters, 4 of the asymmetric Gaussian fit and 2 of the continuum fit. For the Gaussian fit these are the amplitude of a symmetric Gaussian line, the centroid of a symmetric Gaussian line, the width of a symmetric Gaussian line and the value of the exponential tail, called  $\tau$ , which gives a indication of how 'deformed' the Gaussian curve is. For the continuum fit, 2 additional parameters, namely the power-law amplitude and the power-law index, come into play. When the set of starting parameters is already chosen in a way that provides close agreement, the algorithm takes less time to converge.

#### 4.1.2 Error Propagation

If the measured variables  $z_1, z_2, \dots z_N$  are statistically independent of each other, the total deviation can be determined by the formula

$$\Delta h = \sqrt{\Delta z_1^2 \left[ \frac{\partial h}{\partial z_1} \right]^2 + \Delta z_2^2 \left[ \frac{\partial h}{\partial z_2} \right]^2 + \dots + \Delta z_N^2 \left[ \frac{\partial h}{\partial z_N} \right]^2} \quad (7)$$

This is also known as Gaussian error propagation. The squares of the partial derivatives  $\frac{\partial h}{z_1}$ ,  $\frac{\partial h}{z_2}$ , ...,  $\frac{\partial h}{z_N}$  form the weighting factors for the individual measurement uncertainties.

### 4.1.3 Defining Peak Positions

The question how peak positions are actually determined is not unequivocal and defined by the model used for fitting those peak positions. However, the measured data contains uncertainties. If a data set is chosen that contains an approximately Gaussian shaped curve, one is able to fit a model to the data via the Monte Carlo Markov Chain and then display the line centroid, thus the peak position, of the model. The agreement between the model and the data can be displayed through the  $\chi^2$ -value. Figure 8 shows a simulation of data and two fits, one symmetric Gaussian fit and an asymmetric Gaussian fit.

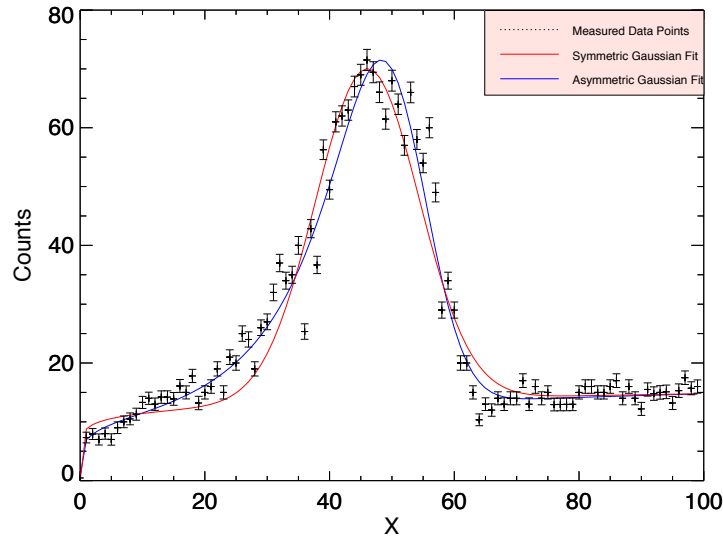


Figure 8: Comparison of symmetric and asymmetric fitting

It is shown that if the data points are distributed non symmetrical, the asymmetric Gaussian fits provides a lower  $\chi^2$ -value. In figure 9 one can see that the  $\chi^2$ -value of

the asymmetric fit is 43.2, the  $\chi^2$ -value of the symmetric fit is 82.1. The improvement will be determined by the  $\chi^2$ -test. The degrees of freedom are 3 for the symmetric Gaussian fit, and 4 for the asymmetric one, since the latter also contains the degradation  $\tau$ , it follows that  $\Delta degrees\ of\ freedom = 1$ . In this case the  $\chi^2$ -test forms to

$$[n]\sigma = \sqrt{\Delta\chi^2} \quad (8)$$

where  $n$  is the value that determines how much more significant in units of  $\sigma$  the  $\chi^2$  is (Press et al. 1995). With  $\Delta\chi^2 = 38.9$  a value of 6.24 for  $n$  is obtained. It can be concluded that the asymmetric fit is 6.24 times 'better' than the symmetric fit in terms of significance and it should rather be used an asymmetric spectral response that can account for degradation.

Figure 9 shows the results of the MCMC fit, the left part shows the fit for the asymmetric Gaussian profile, the right part the symmetric one. Beneath the diagrams, the fitting parameters are displayed, including the  $\chi^2$ -values.

It is to mention that the MCMC is just a fitting routing, it still has to be given the right parameters in order to receive a usable fit. The difference of the line centroids in figure 9 is to highlight. Since the values of the line centroids of the calibration lines are used to fit equation 3 via Curvefit, it makes a difference whether a symmetric or an asymmetric Gaussian fit is used.

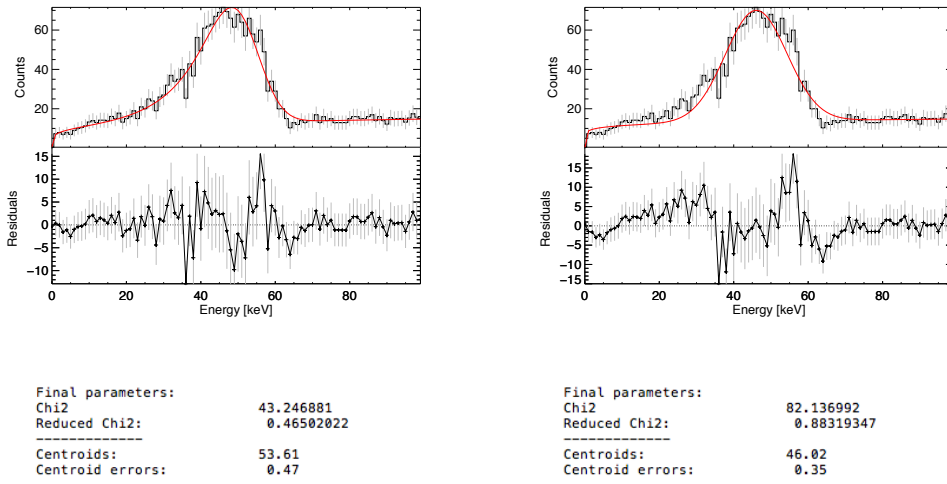


Figure 9: Monte Carlo Markov Chain

#### 4.1.4 Weighting Mean Values

Averaging multiple values that all have statistical uncertainties requires weighting those values with respect to their accuracy. The formula of the weighted mean value is

$$\bar{x} = \frac{\sum_{i=1}^k w_i \cdot x_i}{\sum_{i=1}^k w_i} \quad (9)$$

where the weighting factors  $w_i$  are given by:

$$w_i = \frac{1}{\Delta x_i^2} \quad (10)$$

If all weighting factors  $w_i$  have the same value, then the weighted mean value equals the conventional mean value. The accuracy of the weighted mean value forms to:

$$\Delta \bar{x} = \sqrt{\frac{1}{\sum_{i=1}^k w_i}} \quad (11)$$

(*'Fehlerrechnung TUM'*)

#### 4.1.5 Linear Regression

For the linear regression, which is the task of fitting data to a straight line,  $\chi^2$  can be also used as an indicator of the goodness-of-fit. In this case the equation 4 forms to

$$\chi^2(m, t) = \sum_{i=1}^k \left( \frac{y_i - (m \cdot x_i + t)}{\sigma_i} \right)^2 \quad (12)$$

with

$$L_i = m \cdot x_i + t \quad (13)$$

as the linear function.

As always it is of interest to receive the lowest possible value for  $\chi^2$ . This can be achieved through minimization of equation 12 by derivating it with respect to their parameters  $m$  and  $t$  and calculating where the derivatives vanish. This can be represented by the linear equation system of:

$$0 = \frac{\partial \chi^2}{\partial t} = -2 \sum_{i=1}^k \frac{y_i - (m \cdot x + t)}{\sigma_i} \quad (14)$$

$$0 = \frac{\partial \chi^2}{\partial m} = -2 \sum_{i=1}^k \frac{x_i(y_i - (m \cdot x + t))}{\sigma_i}$$

By rearranging the equation system 14 in a way that  $m$  and  $t$  can be calculated, the best solution for these fit parameters is found (Press et al. 1995). This is used later in chapter 5 and in this case done through Curvefit, a fitting program.

## 4.2 Calibration Procedure

For the calibration, six distinctive lines with well known energy levels are utilized. These are the lines at 23.44 keV, 198.39 keV, 309.88 keV, 584.54 keV, 882.51 keV and 1764.36 keV.

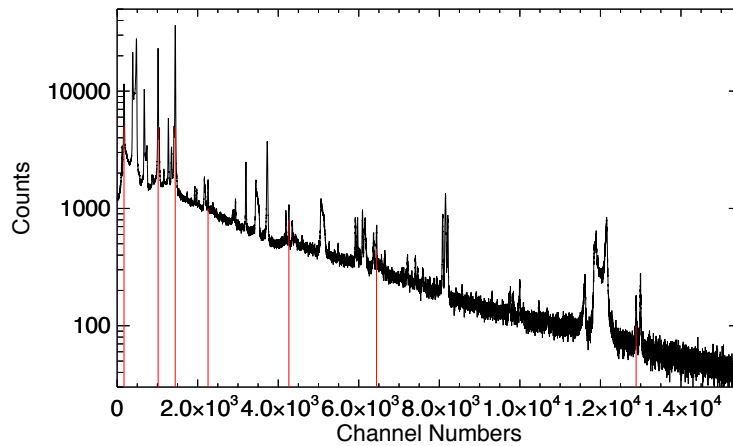


Figure 10: Raw spectrum of detector 0 integrated over a duration of one revolution (revolution 45), the red lines are the energy levels used for calibration

In figure 10, additionally to the six calibration lines, the line with its peak at channel number  $\sim 1025$  (second red line from the left), is shown the diagram. This is the line

we expect to originate from the 139.68 keV transition and because it is also a very dominant line, it should be tested in this thesis if the calibration precision can be increased by utilizing it as a seventh calibration line. After fitting the **asymmetric** Gaussian curves to the data, the line centroid of each of the calibration lines in the channel space is known. These values are of course still with uncertainties. The value of the characteristic energy levels of the transition correspond to the values of these line centroids as shown through the data points in figure 11. With the use of equation 3 the value of the parameters for  $a_0, a_1, a_2, a_3$  can be fitted. After this procedure the energy is now connected to channel numbers by equation 3, the calculated values for the parameters are shown in table 1 and the calibration curve is shown in figure 11.

A fit with the use of equation 3 was computed both with and without the 140 keV line, and also with the 140 keV line instead of the 23 keV line. The results and the  $\chi^2$ -values are shown in table 1 and table 2.

Table 1: Parameters of calibration

	Current calibration	Fitted calibration
$a_0$	-52.95532	$-281.79828 \pm 11.50553$
$a_1$	1.0068996	$1.0527166 \pm 0.0538923$
$a_2$	0.1357609	$0.1357613 \pm 0.0000181$
$a_3$	$-4.74562088 \cdot 10^{-9}$	$(-3.2860452 \pm 1.19679) \cdot 10^{-9}$
$\chi^2$		0.2779

Table 2: Parameters of calibration

	Calibration with the 140 keV line added	Calibration with 140keV instead of 23 keV
$a_0$	$-234.08961 \pm 50.45472$	$-1244.0774 \pm 524.1214$
$a_1$	$0.7538366 \pm 0.2096857$	$1.7966104 \pm 0.5620384$
$a_2$	$0.1358482 \pm 0.0000783$	$0.1356198 \pm 0.0001322$
$a_3$	$(-8.2947258 \pm 5.27523) \cdot 10^{-9}$	$(3.654837 \pm 7.35292) \cdot 10^{-9}$
$\chi^2$	0.5002	0.2235

In figure 11 the calibration function with the use of the parameters of 'Fitted calibration' of table 1 is shown.

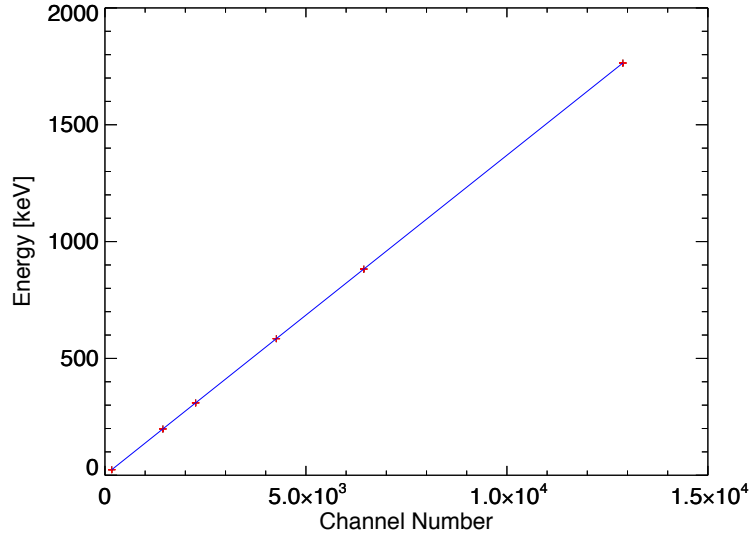


Figure 11: Calibration curve

The error bars are included in figure 11 but since they are barely visible they are shown beneath the diagram in table 3.

Table 3: Correlation of energy to channel

Channel	Energy [keV]	Channel error	Energy error [keV]
176.66	23.44	0.09	0.08
1454.81	198.39	0.01	0.06
2276.10	309.88	0.12	0.07
4298.82	584.54	0.13	0.10
6493.97	882.51	0.15	0.14
12992.55	1764.36	0.34	0.31

The uncertainties of the energy values were calculated via error propagation of equation 3. Furthermore, the uncertainty of  $x$ , thus the uncertainty of the line centroids, is also of interest. With the parameters drawn from the MCMC fit these uncertainties can be calculated. With the use of equation 7 the error propagation forms to

$$\Delta E(x) = \sqrt{\Delta a_0^2 \left[ \frac{\partial E}{\partial a_0} \right]^2 + \Delta a_1^2 \left[ \frac{\partial E}{\partial a_1} \right]^2 + \Delta a_2^2 \left[ \frac{\partial E}{\partial a_2} \right]^2 + \Delta a_3^2 \left[ \frac{\partial E}{\partial a_3} \right]^2} \quad (15)$$

and finally to:

$$\Delta E(x) = \sqrt{\Delta a_0^2 \cdot \left(\frac{1}{x}\right)^2 + \Delta a_1^2 + \Delta a_2^2 \cdot x^2 + \Delta a_3^2 \cdot x^4} \quad (16)$$

In figure 12, the weighting of the individual parameters is illustrated. When equation 3 is decomposed in its summands through  $E(x) = z_1 + z_2 + z_3 + z_4$  with  $z_1 = \frac{a_0}{x}$ ,  $z_2 = a_1$ ,  $z_3 = a_2 \cdot x$ ,  $z_4 = a_3 \cdot x^2$  one can show the proportion of the summands in dependence of  $x$  and therefore the proportion of the parameters  $a_0, a_1, a_2, a_3$  at the calibration function. It can be seen that already above a small channel number, the calibration function is dominated close to a 100 percent by  $z_3$ . From  $z_3 = a_2 \cdot x$  can be followed that  $a_2$  plays a significant role, and  $a_2$  has a fairly good agreement in the three listed calibrations.

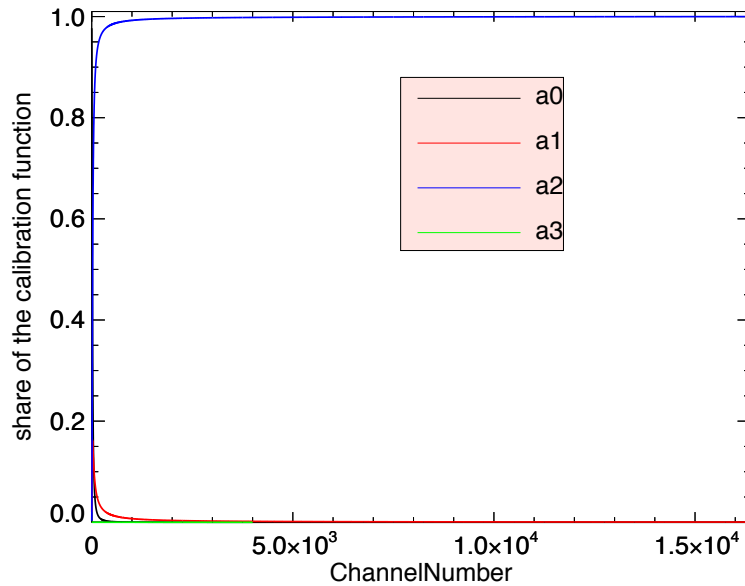


Figure 12: share of the parameters

This shows also that above an already small channel number equation (3) can be seen as approximately linear. This is useful for rough calculation only though, since the calibration has to be as precise as possible.

## 5 Analysis of Data

### 5.1 Comparing Calibrations over Time

In order to do proper fitting for the individual peak positions to the channel numbers, first the range in the channel space has to be defined. Since the peak positions drift to smaller channel numbers over time, this range had to be adapted from time to time.

Table 4: Channel space for fitting the energy levels

	23.44 keV	198.39 keV	309.88 keV	584.54 keV	882.51 keV	1764.36 keV
Start - 22.06.2006	130-210	1435-1495	2250-2310	4260-4340	6450-6550	12900-13040
23.06.2006 - 22.01.2009	130-210	1432-1495	2240-2310	4220-4330	6435-6540	12880-13020
23.01.2009 - 06.01.2013	130-210	1427-1490	2230-2300	4230-4330	6435-6520	12860-13000
07.01.2013 - 26.04.2013	130-210	1427-1490	2240-2310	4230-4330	6420-6475	12860-13000
27.04.2013 - Today	130-210	1427-1490	2240-2310	4230-4330	6420-6475	12810-12950

To illustrate this effect, the drifting is shown for the 882 keV line. The channel space used for fitting the peak is drawn into the diagram for revolution 50, 500, 950 and 1400. It is striking that the range of the channel space has also been adjusted. In revolution 50 the range extends over 100 channel numbers, whereas in revolution 1400 it extends only over 55. The different height of the underlying continuum has its origin in the varying activity of the sun, that behaves anti-cyclically to the amount of the continuum. The fact that the peak positions of the spectra drift steadily to the lower end of the channel space is owed to the decrease of detection efficiency over time.

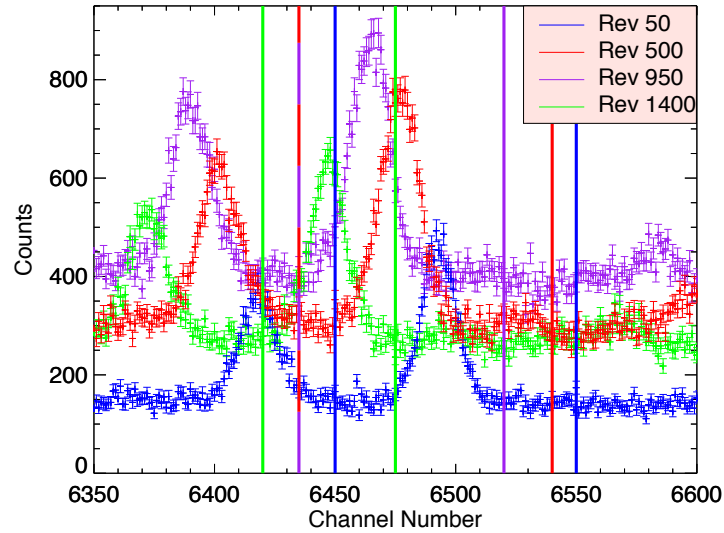


Figure 13: Calibration windows for different time periods

## 5.2 Calibration Adjustments

The effects shown in the previous section require that the parameters of the calibration function have to be continuously adjusted. The characteristic energy levels do not change, since they are given by nature, but the channel numbers they are measured in do. In figure 14 the calibration curve of revolution 45 is used as a base line calibration curve, since it was one of the first utilized revolutions, and is subtracted from calibration curves of different revolutions.

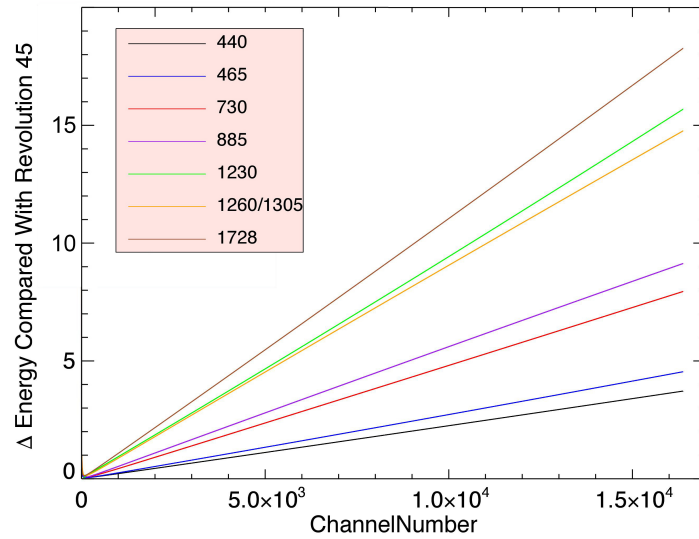


Figure 14: (Curve of revolution  $n = E^n(ch) - E^{45}(ch)$ )

Figure 15 displays this effect more vivid for the six calibration lines. The different energy levels of revolution 45, one of the first revolutions, and revolution 1728, one of the latest revolutions, are compared.

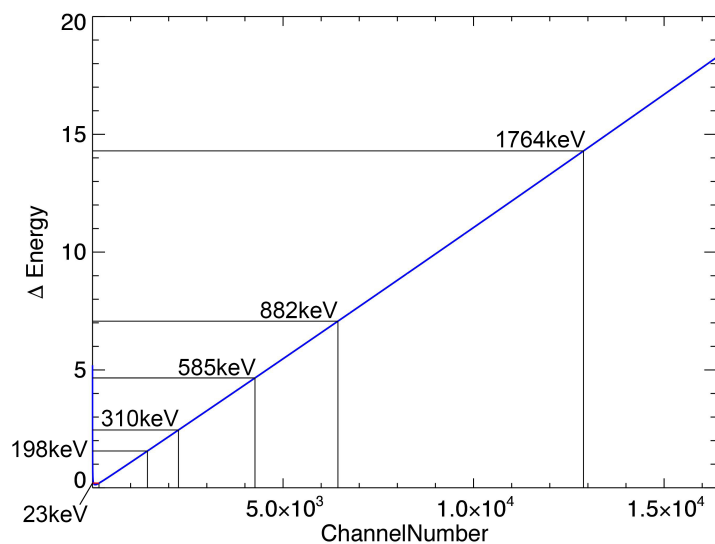


Figure 15: Difference of the calibration curves of revolution 45 and 1728

The proportion of  $\Delta$ Energy to the absolute energy values is about  $\sim 0.8\%$ , as for example the difference between revolution 45 and 1728 in the 1764 keV line is  $\sim 14.2$  keV. This demonstrates the importance of adjusting the parameters. This is about 5 times the value of SPI's stated energy resolution of 2.2 keV at 1.33 MeV, which is exactly the reason why the calibration parameters are readjusted every revolution. The  $\sim 0.8\%$  apply to all energies except the very small ones, where the linear part does not yet dominate the function. The analysis here is that the detector degradation is continuously increasing.

### 5.3 Characteristics of the Peak Positions

It was shown in chapter 4 which precautions have to be taken to carry out the calibration successfully. After this, the calibrated data of interest can be analysed in energy space. In the following, this was done with the calibrations from ISDC. The energies of the line peaks have been analysed and their value per revolution was recorded. When looking at the shift of the peak positions in the data one can see that for various energy levels the behaviour differs. For a single measurement period, peak positions show a shift to higher energy values for some lines, like 438 keV, 1778 keV (figure 16) or 1764 keV (figure 17, shown later). In other energies this effect can not be seen, or not as clear, for example for 23 keV and 1633 keV.

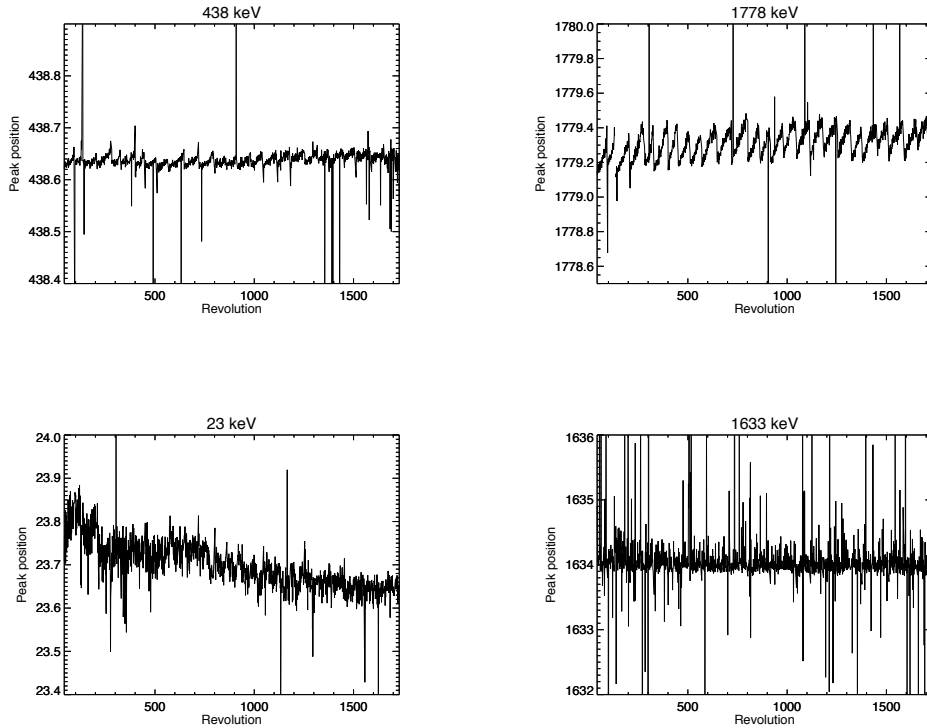


Figure 16: Measured peak position values of different energy levels

#### 5.4 Line Identification

The lines that were examined in the previous section are subject to different physical processes. Those lines as well as other lines from the spectrum with comparatively high count rates are listed in table 5. Most of the lines originate from radioactive decays, especially within the germanium crystals. The count rates were recorded in 2003, during the revolutions 49, 50, 51 and 53.

Table 5: Strong energy levels with respect to their count rate (Weidenspointner et al. 2003)

Nominal energy [keV]	Parent process	Count rate [cts/s]
23.44	$^{71m}\text{Ge}(IT)^{71}\text{Ge}$	3.44
139.68	$^{75m}\text{Ge}(IT)^{75}\text{Ge}$	30.26
198.39	$^{71m}\text{Ge}(IT)^{71}\text{Ge}$	50.63
309.88	$^{67}\text{Ga}(EC)^{67m}\text{Zn} + K$	1.207
438.62	$^{69m}\text{Zn}(IT)^{69}\text{Zn}$	2.75
511.00	positron annihilation	1.73
584.54	$^{69}\text{Ge}(EC)^{69}\text{Ga} + K$	1.051
752.1	$^{204m}\text{Bi}(IT)^{204}\text{Bi}$	0.198
817.89	$^{58}\text{Co}(EC)^{58}\text{Fe} + K$	0.754
882.51	$^{69}\text{Ge}(EC)^{69}\text{Ga} + K$	0.744
1107.01	$^{69}\text{Ge}(EC)^{69}\text{Ga}$	0.92
1117.26	$^{69}\text{Ge}(EC)^{69}\text{Ga} + K$	1.79
1460.82	$^{40}\text{K}(EC)^{40}\text{Ar}$	0.114
1764.36	$^{205}\text{Bi}(EC)^{205}\text{Pb}$	0.222

Apart from the positron annihilation line, two types of physical processes can be seen. **E**lectron **C**apture (EC) is a process, in which a proton rich atom converts a proton to a neutron by capturing an electron. Thereby a neutrino is emitted, that carries the entire decay energy and has thus a characteristic energy for the particular process, according to the schema:



IT means isometric transition, which occurs after an isobaric transition, from which the radioactive nucleus has too much energy left. The isobaric transition can originate from electron capture, positron emission or beta emission. The isometric transition has its name because the reactant and the product are isomers. The reactant converts to the product by dropping to the ground state, emitting energy in form of gamma-rays.

### 5.5 Correlation of Energy and Increasing Values of Peak Positions

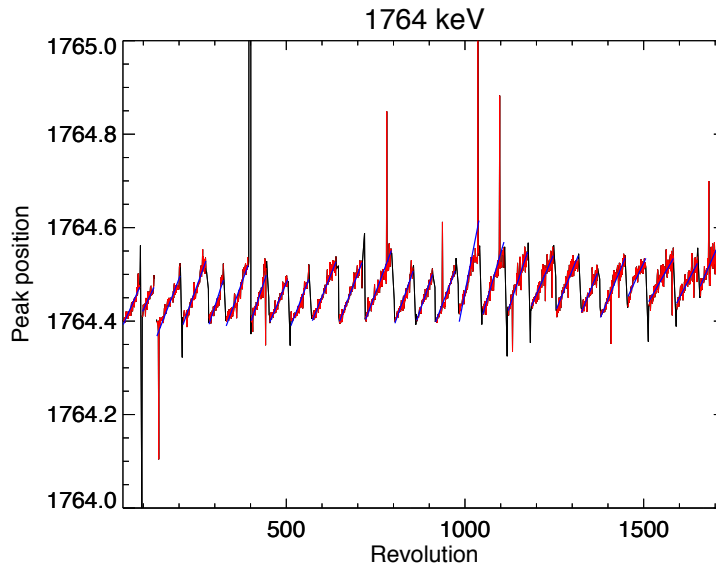


Figure 17: Slopes of the peak position values

In figure 17 one can see the effect of the annealing phases, when the measured peak positions concurs with the lab line energy. In between these phases one can see a linear increase of the peak position values. The individual slopes [keV/revolution] of those measurement periods were taken and their mean value calculated according to chapter 4.1.4.

According to this procedure, the peaks of a few energy levels, namely 140 keV, 198 keV, 310 keV, 438 keV, 511 keV, 583 keV, 662 keV, 752 keV, 882 keV, 1107 keV, 1312 keV, 1332 keV, 1764 keV, 1778 keV were looked at and the mean value of their slopes plotted against their energy value. It can be seen in figure 18 that the slopes get steeper with increasing energy. This is illustrated through another linear fit, thus a slope of the slopes [(keV/revolution)/keV].

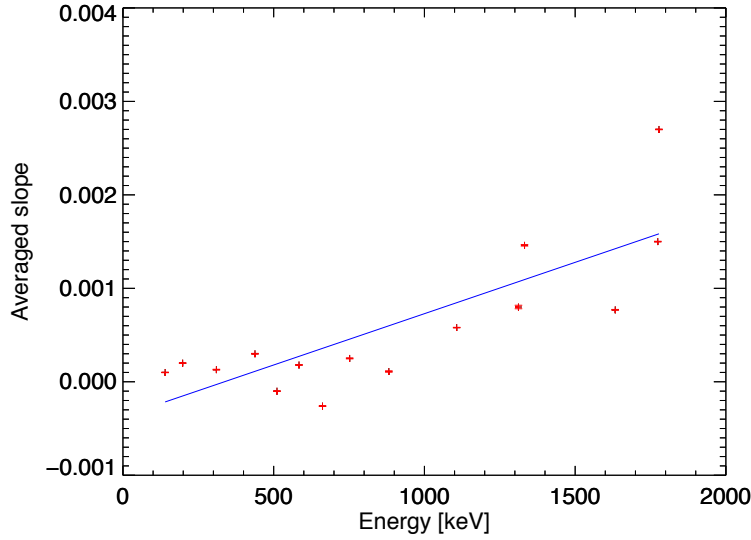


Figure 18: Slopes plotted against energy of line transitions

This effect is relevant when looking at the Doppler shift, and as shown by

$$\text{Doppler shift} \left[ \frac{km}{s} \right] = \frac{E_{lab} - E_{measured}}{E_{lab}} \cdot c \quad (18)$$

a bigger discrepancy between the lab line energy and the measured energy results in a bigger Doppler shift. This means the size of the Doppler shift is increasing faster for higher energies, since the peak position values of higher energies move faster away from the lab line energy during the measurement periods. When looking at figure 17 as an example, in almost every measurement period a value of  $\sim 1764.5$  keV is being measured at one point. With the nominal energy of 1764.36 keV (table 5), this corresponds to velocities of  $\sim 23.8 \frac{km}{s}$ . These systematic uncertainties need to be added for each measurement. When looking beyond the Doppler shift at the Doppler broadening, this effect is particularly important for example for the investigation of the  $^{26}\text{Al}$  line mentioned in chapter 2.2.

## 6 Conclusion

This thesis should give an insight into the INTEGRAL mission and gamma-ray detection, and in particular the work with the Spectrometer SPI. It has been shown which precautions have to be taken for a satellite mission, how the gamma rays can be detected and which challenges have to be faced in the analysis of the measured data. Above that, it was shown how a semiconductor detector works in general and which adjustments have to be made in order to operate germanium detectors in space.

Fitting models as close as possible to data is a difficult task, however unavoidable to use the obtained data for further analysis. A carefully executed calibration is also essential for data analysis. In addition, the background radiation has to be carefully considered when the universe should be observed and data are to be extracted from the sky. Only after all this is done, the main task, studying the behaviour of gamma-rays, can be achieved. For further research on gamma radiation, satellite missions are indispensable since no usable measurements can be made on earth, owed the gamma-ray absorbing nature of earth's atmosphere.

By working on this thesis, some conclusions could be drawn. It was shown that adding another calibration line to the six given calibration lines would not improve the accuracy of the calibration function.

In the past the INTEGRAL Science Data Centre was responsible for the energy calibration. In order to calculate the necessary peak positions of the calibration lines they have used symmetric Gaussian fits. It was shown that an asymmetric Gaussian fits provides closer agreement to the data, especially when the degradation is bigger. This can be proven through the  $\chi^2$ -value. It can be followed that a energy calibration procedure utilizing asymmetric Gaussian fits would be more accurate than the current method. In the future this will be even more important, since the detector efficiency will only decrease with given time, leading to even larger degradations of the peaks. This is particularly important for higher energies, that show higher degradation due to effects of Poisson distribution. It was also shown that the measurements generally do not agree exactly with theoretical values, and this effect and the consequences were shown through investigation of the peak positions of some strong lines and their behaviour during measuring phases.

Despite 4 detector breakdowns, SPI still works excellent, as well as the satellite itself, and the mission could be extended for many more years, until eventually the fuel runs out. But even then the work will continue, since SPI has provided even now a legacy database for gamma-ray spectroscopy.

## 7 Danksagung

An dieser Stelle möchte ich mich als erstes bei Professor Roland Diehl für die Möglichkeit bedanken, meine Bachelorarbeit am Max-Planck-Institut für Extraterrestrische Physik zu schreiben. Es hat mir großen Spaß gemacht, mich zum erstmal 'richtig' an die Wissenschaft heranzutasten. Ein riesiges Dankeschön geht an meine Betreuer Christoph Weinberger und Thomas Siegert, die immer mit Rat und Tat zur Seite standen. Ich konnte immer auf ein offenes Ohr zählen, und habe stets kompetente Beratung erhalten. Vermutlich war das Ganze nicht immer einfach für euch, also Danke! Außerdem möchte ich mich bei meinem 'Leidens'genossen Markus Trost bedanken, der eine große Bereicherung für mein Wohlbefinden beim Schreiben dieser Arbeit war.

## References

- Diehl, R. (2013). “Nuclear astrophysics lessons from INTEGRAL”. In: *Reports on Progress in Physics* 76.2, 026301, p. 026301. DOI: 10.1088/0034-4885/76/2/026301. arXiv: 1302.3441 [astro-ph.HE].
- Eckert, D. et al. (2008). “INTEGRAL discovery of non-thermal hard X-ray emission from the Ophiuchus cluster”. In: *Astronomy and Astrophysics* 479, pp. 27–34. DOI: 10.1051/0004-6361:20078853. arXiv: 0712.2326.
- inthehelp@sciops.esa.int. *Anti Coincidence Shield*. [http://www.isdc.unige.ch/integral/download/osa/doc/10.1/osa\\_um\\_spi/node15.html](http://www.isdc.unige.ch/integral/download/osa/doc/10.1/osa_um_spi/node15.html). Accessed: 23.08.2017.
- Knoll, Glenn F. (2012). *Radiation Detection and Measurement*. Wileys, 437, 424. ISBN: 978-0-470-13148-0.
- Kretschmer, K. et al. (2013). “Kinematics of massive star ejecta in the Milky Way as traced by  $^{26}\text{Al}$ ”. In: *A&A* 559, A99, A99. DOI: 10.1051/0004-6361/201322563. arXiv: 1309.4980 [astro-ph.HE].
- Press, William H. et al. (1995). *Numerical Recipes in Fortran 77 The Art of Scientific Computing Second Edition Volume 1 of Fortran Numerical Recipes*. Press Syndicate of the University of Cambridge. ISBN: 0-521-43064-X.
- TU-Muenchen. *Fehlerrechnung TUM*. <https://www.ph.tum.de/academics/org/labs/ap/org/ABW.pdf>. Accessed: 03.09.2017.
- Vedrenne, G. et al. (2003). “SPI: The spectrometer aboard INTEGRAL”. In: *Astronomy and Astrophysics* 411, pp. L63–L70. DOI: 10.1051/0004-6361:20031482.
- Wang, W. et al. (2009). “Spectral and intensity variations of Galactic  $^{26}\text{Al}$  emission”. In: *A&A* 496, pp. 713–724. DOI: 10.1051/0004-6361/200811175. arXiv: 0902.0211 [astro-ph.HE].
- Weidenspointner, G. et al. (2003). “First identification and modelling of SPI background lines”. In: *Astronomy and Astrophysics* 411, pp. L113–L116. DOI: 10.1051/0004-6361:20031209.
- Winkler, C. et al. (2003). “The INTEGRAL mission”. In: *A&A* 411, pp. L1–L6. DOI: 10.1051/0004-6361:20031288.

## List of Figures

1	Integral spacecraft . . . . .	3
2	illustration of the Spectrometer aboard INTEGRAL . . . . .	5
3	picture of the detector array aboard INTEGRAL . . . . .	6
4	Full Width at Half Maximum . . . . .	7
5	Comparison of good and poor resolution . . . . .	8
6	Detector breakdowns . . . . .	9
7	Picture of the cryostat aboard INTEGRAL . . . . .	9
8	Comparison of symmetric and asymmetric fitting . . . . .	15
9	Monte Carlo Markov Chain . . . . .	16
10	Raw spectrum of detector 0 integrated over a duration of one revolution (revolution 45), the red lines are the energy levels used for calibration . . . . .	18
11	Calibration curve . . . . .	20
12	share of the parameters . . . . .	21
13	Calibration windows for different time periods . . . . .	23
14	<i>(Curve of revolution <math>n = E^n(ch) - E^{45}(ch)</math>)</i> . . . . .	24
15	Difference of the calibration curves of revolution 45 and 1728 . . . . .	25
16	Measured peak position values of different energy levels . . . . .	26
17	Slopes of the peak position values . . . . .	28
18	Slopes plotted against energy of line transitions . . . . .	29

**List of Tables**

1	Parameters of calibration . . . . .	19
2	Parameters of calibration . . . . .	19
3	Correlation of energy to channel . . . . .	20
4	Channel space for fitting the energy levels . . . . .	22
5	Strong energy levels with respect to their count rate (Weidenspointner et al. 2003) . . . . .	27